Journal of Materials Chemistry A

PAPER

View Article Online
View Journal | View Issue

Cite this: J. Mater. Chem. A, 2019, 7, 21362

A new P2-type layered oxide cathode with superior full-cell performances for K-ion batteries†

Jang-Yeon Hwang, ‡[a] Jongsoon Kim, ‡[b] Tae-Yeon Yu,[a] Hun-Gi Jung,[c] JaeKook Kim,[d] Kwang-Ho Kim[e] and Yang-Kook Sun *[a]

Received 19th July 2019
Accepted 22nd August 2019

DOI: 10.1039/c9ta07837a

rsc.li/materials-a

K-ion batteries (KIB) have attracted considerable attention as a potential alternative to Li-ion batteries because of their low cost and high energy density. However, their development and durability have been severely limited by the lack of suitable cathodes with high capacity and good cycle life. Here, we prepare a low-cost Mn-based layered oxide, P2-type $K_{0.75}[Mn_{0.8}Ni_{0.1}Fe_{0.1}]O_2$ (P2-$K_{0.75}MNFO_2$), *via* an electrochemical ion-exchange process and demonstrate its excellent K storage performance as a cathode for KIBs. During the charge–discharge process, P2-$K_{0.75}MNFO_2$ can release and store considerable amounts (~0.5 mol) of K^+ ions without multiple phase transitions in the voltage range of 1.5–3.9 V (*vs.* K/K^+), as verified by X-ray diffraction characterization and first-principles calculations. Owing to its highly stable layered oxide framework, P2-$K_{0.75}MNFO_2$ delivers a high reversible capacity of 110 mA h g^{-1} at 0.1C and exhibits an outstanding cycle retention of 70% over 200 cycles at both 1C and 10C. In addition, a full cell with P2-$K_{0.75}MNFO_2$ as the cathode and hard carbon as the anode demonstrates long-term cycling stability over 1000 cycles, illustrating the feasibility of a safe and practical KIB system.

Introduction

Recently, development of mid- to large-scale energy storage systems has accelerated rapidly because of the strong need for stable energy supplies and the aggressive promotion of electric vehicle applications worldwide.[1] To date, Li-ion batteries (LIBs) have been successfully used as the main power supply for applications ranging from portable electronics to grid-scale energy storage devices, which are considered indispensable to daily life.[2] With the explosive growth of the LIB market, however, the global reserves of lithium are anticipated to become depleted in the near future; consequently, a sharp rise in the production cost will be inevitable.[3] Concerns surrounding the scarcity of lithium resources have resulted in development of new types of electrical energy storage systems.[4,5] K-ion batteries (KIBs), which operate under a "rocking-chair" K storage mechanism similar to that of Li in LIBs, has been emerging as an attractive alternative to LIBs considering the abundance of K resources.[6] In addition, potassium, the next alkali metal after sodium in the periodic table, provides a lower reduction potential than sodium (K: −2.93 V, Na: −2.71 V *vs.* the standard hydrogen electrode (SHE)), allowing higher energy density for KIBs.[7] In addition, it was found that K^+ ions intercalate into carbonaceous anodes such as graphite and hard carbon; accordingly, KIBs[8–10] will also undoubtedly be cost-effective and safe and have greater potential for practical applications using the existing industrial system for LIBs.[11–13] Hence, various electrode materials are being introduced.[14–17]

Layered transition metal oxides, P2- or P3-type K_xMO_2 (M = transition metal), appear to be promising cathode materials for KIBs. A few studies on P2- and P3-type materials showed reversible K-ion storage performance;[10,18–20] however, K^+ ions (1.38 Å) are larger than Li^+ ions (0.76 Å) and Na^+ ions (1.02 Å), so irreversible multiple phase transitions are usually generated during K-ion de/intercalation, resulting in poor rate capability and severe capacity fading.[7] Therefore, a rational structural design of layered transition metal oxide materials is required to facilitate the K-ion reaction kinetics and improve the durability of KIBs. On the other hand, studies on K-ion full cells using K-metal free anodes are still in their infancy; thus, their development and sustainability that can compete with current LIBs have been severely limited.

In this study, we developed a novel and low-cost Mn-based layered oxide cathode material, P2-type $K_{0.75}[Mn_{0.8}Ni_{0.1}Fe_{0.1}]O_2$ (P2-$K_{0.75}MNFO_2$), that can deliver superior potassium

[a]Department of Energy Engineering, Hanyang University, Seoul 04763, Republic of Korea. E-mail: yksun@hanyang.ac.kr

[b]Department of Nanotechnology and Advanced Materials Engineering, Sejong University, Seoul 05006, Republic of Korea

[c]Center for Energy Storage Research, Green City Technology Institute, Korea Institute of Science and Technology, Hwarang-ro 14 gil 5, Seongbuk-gu, Seoul 02792, Republic of Korea

[d]Department of Materials Science and Engineering, Chonnam National University, Gwangju 500-757, Republic of Korea

[e]School of Materials Science and Engineering, Pusan National University, Busan, 46241, Republic of Korea

† Electronic supplementary information (ESI) available. See DOI: 10.1039/c9ta07837a

‡ Jang-Yeon Hwang and Jongsoon Kim equally contributed to this work.

storage performance with smooth electrochemistry. On the basis of the stoichiometry of sodium and transition metals, recently, our group developed a P2-type Mn-rich layered oxide cathode, $Na_{0.55}[Mn_{0.8}Ni_{0.1}Fe_{0.1}]O_2$ (P2-$Na_{0.55}MNFO_2$), by partially substituting Ni and Fe into the Mn sites. A highly stable layered oxide framework of P2-$Na_{0.55}MNFO_2$ enabled high capacity and excellent cycling stability by suppressing the structural transitions during multiple charge–discharge processes. Inspired by previous findings, we used P2-$Na_{0.55}MNFO_2$ as an efficient precursor for synthesizing a high-performance Mn-rich based layered oxide cathode.[21] By using the electrochemical ion-exchange method,[22] P2-$K_{0.75}MNFO_2$ was successfully synthesized from P2-$Na_{0.55}MNFO_2$, and its electrochemical properties and reaction mechanism were investigated through combined studies using first-principles calculations and various experiments. The key feature of the proposed cathode is the presence of sufficient diffusion pathways for large K^+ ions in the structure. P2-$K_{0.75}MNFO_2$ has large two-dimensional K^+ diffusion paths and thus undergoes little structural change without the extent of multiple phase transitions in the voltage range of 1.5–3.9 V (*vs.* K/K^+). As a result, P2-$K_{0.75}MNFO_2$ demonstrated a high specific capacity of 110 mA h g^{-1}, outstanding cycling stability, and excellent power capability. Notably, a proposed full cell with a P2-$K_{0.75}MNFO_2$ cathode and hard carbon anode integrated state-of-the-art developments in KIB technology, delivering an extremely long cycling performance over 1000 cycles that has not yet been reported to the best of our knowledge.

Experimental

Synthesis of cathode materials: P2-$Na_{0.55}[Mn_{0.8}Ni_{0.1}Fe_{0.1}]O_2$ and P2-$K_{0.75}[Mn_{0.8}Ni_{0.1}Fe_{0.1}]O_2$

The P2-$Na_{0.55}[Mn_{0.8}Ni_{0.1}Fe_{0.1}]O_2$ (P2-$Na_{0.55}MNFO_2$) cathode material was prepared by a typical solid-state method. For the solid-state reaction, stoichiometric amounts of sodium carbonate, manganese(II) acetate tetrahydrate, nickel(II) acetate tetrahydrate, and iron(II) acetate were mixed according to the desired Na : Mn : Ni : Fe ratio (0.55 : 0.8 : 0.1 : 0.1). The mixed powders were calcined at 950 °C for 12 h in an O_2 atmosphere and then quenched in an O_2 atmosphere. The P2-$K_{0.75}[Mn_{0.8}Ni_{0.1}Fe_{0.1}]O_2$ (P2-$K_{0.75}MNFO_2$) cathode was prepared *via* an electrochemical ion-exchange process of P2-$Na_{0.55}MNFO_2$. The P2-$Na_{0.55}MNFO_2$ was subjected to 20 cycles in a K metal|-ethylene carbonate (EC)/diethylene carbonate (DEC) (1 : 1, v/v)| P2- P2-$Na_{0.55}MNFO_2$ cell at a current rate of 0.1C (10 mA g^{-1}) in the voltage range of 1.5–3.9 V.

Material characterization

The morphologies of the powders were examined using scanning electron microscopy (SEM; JSM-6340F, JEOL). Transmission electron microscopy (TEM; JEM2010, JEOL) and energy-dispersive X-ray spectroscopy (EDX) mappings were used to determine the localized particle morphologies and confirm the stoichiometry of the P2-$Na_{0.55}MNFO_2$ compound and P2-$K_{0.75}MNFO_2$. *Ex situ*, *in operando* and powder X-ray diffraction (XRD) (Empyrean, Panalytical) using Cu Kα radiation was employed to identify the crystalline phases of the materials. XRD data were obtained in the 2θ range of 10–80° at a step size of 0.03°. To avoid exposure to air or moisture, we used a ketone-sealed apparatus for the XRD measurements. The XRD data were refined by the Rietveld method using FullProf software. X-ray photoelectron spectroscopy (XPS, PHI5600, PerkinElmer, USA) measurements were performed in macro mode (3 mm × 3 mm). During XPS measurements, the samples were first transferred into a hermetically sealed transfer chamber in a glovebox and then transferred into the vacuum chamber of the XPS machine, preventing exposure to air or water.

Electrochemical characterization

The cathodes were fabricated by blending the P2-$Na_{0.55}MNFO_2$ active mass (85 wt%), Super-P carbon black (10 wt%), and polyvinylidene fluoride (5 wt%). The resultant slurry was uniformly pasted onto aluminum foil using the doctor blade method and then carefully dried at 110 °C for 12 h under vacuum. The loading of the active mass on the foils was approximately 3.0–4.0 mg cm^{-2}. Electrochemical characterization was performed using 2032 coin half-cells. The electrolyte solution used in this study was 0.5 M KPF_6 in EC and DEC (1 : 1 v/v). The fabricated cathodes and potassium metal anodes were separated by a glass fiber (Advantec) to prevent short-circuiting. All the cells were prepared in an Ar-filled dry box. A typical galvanostatic charge–discharge test was performed in the range of 1.5–3.9 V *vs.* K/K^+ for the half-cell, where 1C = 100 mA g^{-1}. The galvanostatic intermittent titration technique (GITT) was applied at each 15 min charge (depotassiation)/discharge (potassiation) step, followed by a 1 h relaxation step. The anode was fabricated by blending the hard carbon active mass (80 wt%), Super-P carbon black (10 wt%) and polyacrylic acid (dissolved in water) (10 wt%). The resultant slurry was uniformly pasted onto Cu foil using the doctor blade method and then carefully dried at 80 °C for 12 h under vacuum. To remove irreversible capacity in the first cycle, the hard carbon anode was recycled in the voltage range of 0.01–2.0 V for two cycles before the hard carbon/P2-$K_{0.75}MNFO_2$ full cell was fabricated. Full cell balance was achieved by maintaining the capacity ratio of the anode to the cathode (N/P ratio) at 1.2 : 1.

Theoretical calculation details

All the density functional theory calculations were performed using the Vienna *Ab initio* Simulation Package (VASP).[23] We used projector-augmented wave pseudopotentials[24] with a plane-wave basis set as implemented in VASP. Perdew–Burke–Ernzerhof parametrization of the generalized gradient approximation (GGA) was used for the exchange–correlation functional.[25] The GGA+*U* method[26] was adopted to address the localization of the d orbital in Mn, Fe, and Ni ions, with *U* values of 3.9, 4.0, and 6.0 eV, which are used in the previous report.[27] All calculations were performed with an energy cut-off of 500 eV until the remaining force in the system converged to less than 0.05 eV $Å^{-1}$ per unit cell. The cluster-assisted statistical mechanics (CASM) software[28] was used for the generation of all K/vacancy

configurations for each composition and 30 configurations with the lowest electrostatic energy for each composition were used for DFT calculation. Nudged elastic band (NEB) calculations[29] were performed to determine the activation barrier of K^+ ion diffusion in the P2-$K_x[Mn_{0.8}Ni_{0.1}\ Fe_{0.1}]O_2$ structure. A unit cell consisting of four formula units of P2-$K_x[Mn_{0.8}Ni_{0.1}Fe_{0.1}]O_2$ was used, and one K^+/vacancy arrangement was generated to model the K^+ ion diffusion. During the NEB calculation, all the structures were allowed to relax within the fixed lattice parameters.

Results and discussion

In order to obtain a P2-type $K_x[Mn_{0.8}Ni_{0.1}Fe_{0.1}]O_2$ (P2-K_x-$MNFO_2$), we first synthesized P2-type $Na_{0.55}[Mn_{0.8}Ni_{0.1}Fe_{0.1}]O_2$ (P2-$Na_{0.55}MNFO_2$) as a precursor material *via* a typical solid-state route. The obtained X-ray diffraction (XRD) patterns of the material revealed a P2-type layered hexagonal structure with $P6_3/mmc$ symmetry, as shown in Fig. S1.†[23] The atomic ratio of Na : Mn : Ni : Fe = 0.55 : 0.8 : 0.1 : 0.1 was confirmed by inductively coupled plasma optical emission spectrometry (ICP-OES) of the final product (Table S1†). Transmission electron microscopy (TEM) images of P2-$Na_{0.55}MNFO_2$ show hexagonal micrometric particles with average diameters of 1–5 μm (Fig. S2a†). TEM-EDX analyses further confirmed that the atomic ratio of P2-$Na_{0.55}MNFO_2$ was Na : Mn : Ni : Fe = 0.55 : 0.8 : 0.1 : 0.1 (Fig. S2b†).

The electrochemical ion-exchange process was used to transform the P2-$Na_{0.55}MNFO_2$ into P2-K_xMNFO_2 in a K metal|0.5 M KPF_6 dissolved in ethylene carbonate (EC)/diethylene carbonate (DEC) = 1 : 1|P2-$Na_{0.55}MNFO_2$ cell in the voltage range of 1.5–3.9 V (*vs.* K/K^+) (Fig. S3†). During the first desodiation process, ~0.3 mol Na ions were extracted from the P2-$Na_{0.55}MNFO_2$ structure, corresponding to an initial charge capacity of ~75 mA h g^{-1}. During the subsequent first discharge process (potassiation) to 1.5 V, K^+ ions were progressively intercalated into $Na_{0.25}MNFO_2$, and a discharge capacity of ~115 mA h g^{-1} was reached. After the first desodiation process, the (002) and (004) diffraction peaks of the sodium-based P2 (Na-P2) phases shifted toward lower angles (Fig. 1a), in good agreement with a previous report on a P2-type layered oxide cathode.[30] After intercalating the K ions into the structure, the (002) and (004) diffraction peaks of the potassium-based P2 (K-P2) phases are located at lower angles than Na-P2 phases, indicating an increase in the *c* lattice parameter resulting from intercalation of K ions, which are larger than Na ions, into the structure. After discharge to 2.5 V, the intensity of the (002) diffraction peak of the Na-P2 phase was greatly reduced, and the (004), (100), (102), (103), and (104) peaks (Na-P2 phases) became broader. On the other hand, intense new (002) and (004) peaks in the K-P2 phase appeared around 14° and 28.2°, respectively. In addition, new (100), (102), (103), and (104) peaks corresponding to the K-P2 phase also appeared.[31] These changes in the peaks in the XRD patterns indicate the initial potassium intercalation into the $Na_{0.25}MNFO_2$ structure with a Na/K biphasic transition.[20] After further discharging to 2.0 V, the intensity of all the diffraction peaks in the K-P2 phase became stronger. At the end of the discharge process (1.5 V), except for

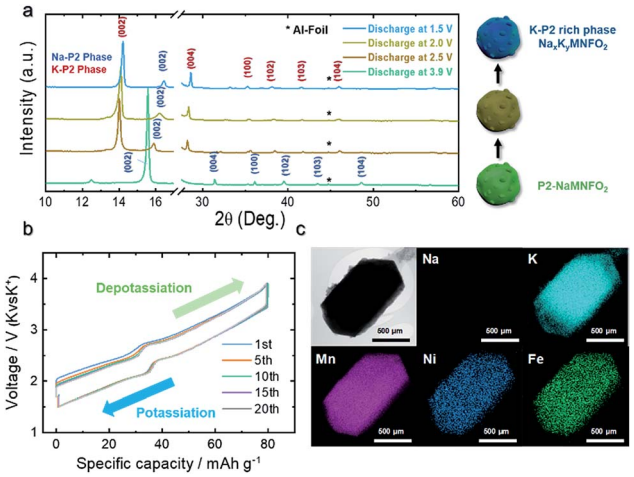

Fig. 1 (a) Electrochemical ion exchange process in the first cycle: *ex situ* XRD patterns of the $Na_xK_yMNFO_2$ electrode in different states of charge. (b) Galvanostatic charge–discharge profiles of the Na_xK_y-$MNFO_2$ electrode at the 1st, 5th, 10th, 15th and 20th cycle in the voltage range of 1.5–3.9 V. (c) TEM image with EDX maps of P2-$K_{0.75}MNFO_2$.

the (002) peak at approximately 16.3°, the XRD peaks corresponding to the Na-based P2-phase almost disappeared, whereas the main K-based P2-phase became more pronounced. The *ex situ* XRD data clearly shows that the main crystal structure of the material obviously changed from that of the Na-P2 phase to that of the K-P2 phase during the first potassiation process. To obtain the pure P2-phase K_xMNFO_2 compound, a further ion-exchange process was conducted under the same conditions. During several charge–discharge processes for 20 cycles (Fig. 1b), the galvanostatic charge–discharge voltage profiles changed continuously and the overpotential became smaller; this may imply that the electrochemical Na^+/K^+ ion exchange was nearly completed. As shown in a SEM image (Fig. S4†), the particle shape of K_xMNFO_2 was maintained after the electrochemical ion-exchange process.

Elemental analyses by TEM-EDX mapping of P2-K_xMNFO_2 proved that the Na^+ ions in $Na_{0.25}MNFO_2$ were obviously exchanged for K^+ ions (Fig. 1c). The measured atomic ratio of K, Fe, Ni, and Mn in P2-K_xMNFO_2 was determined to be 0.75 : 0.8 : 0.1 : 0.1 (P2-$K_{0.75}MNFO_2$), in good agreement with the ICP analysis result in Table S2.† The structure of P2-$K_{0.75}MNFO_2$ was analyzed by Rietveld refinement based on the XRD pattern. As shown in Fig. 2a, it was verified that the lattice parameters of P2-$K_{0.75}MNFO_2$ with the space group $P6_3/mmc$ were a = 2.93780(9) Å and c = 12.5301(1) Å. The detailed structural information of P2-$K_{0.75}MNFO_2$, such as the atomic positions, B_{iso}, and occupancy, is given in Table S3.† The small reliability factors (R_P = 5.76%, R_I = 4.37%, R_F = 8.81%, χ^2 = 4.04%) indicate the high accuracy of Rietveld refinement data of P2-$K_{0.75}MNFO_2$. Note that the atomic position of K^+ ions in P2-$K_{0.75}MNFO_2$ could be similar to that of Na^+ ions in P2-Na_x-$MNFO_2$. The bond valence sum (BVS) energy map of P2-$K_{0.75}MNFO_2$ (Fig. 2b) revealed the large two-dimensional K^+ diffusion paths between MO_6 octahedra (M: Fe, Ni, Mn); this property is highly advantageous for enhancing the cycling

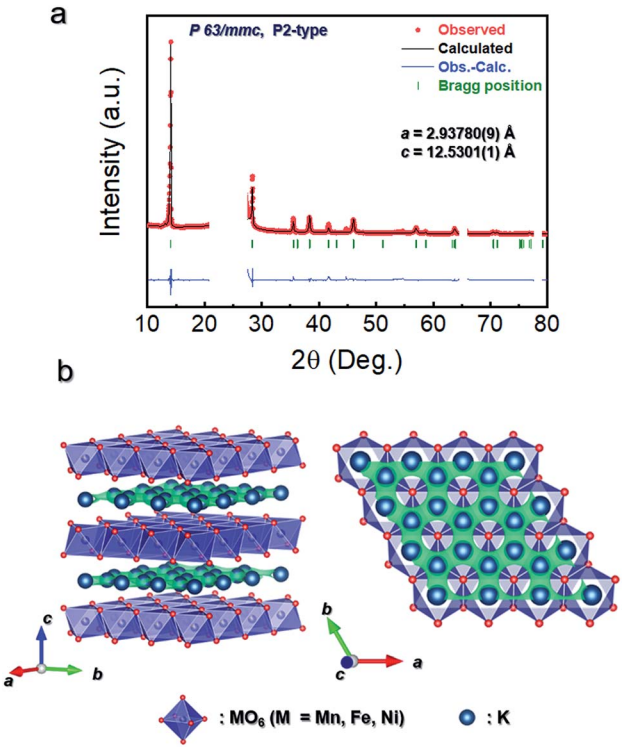

Fig. 2 (a) Refined XRD pattern of P2-$K_{0.75}MNFO_2$ (R_P = 5.76%, R_I = 4.37%, R_F = 8.81%, χ^2 = 4.04%; the XRD peaks associated with the air-protective film and Al foil were excluded), and (b) BVS energy map of P2-$K_{0.75}MNFO_2$ with possible K^+ ion sites in the structure.

stability and power capability when it accommodates a large size K^+ ion into its crystal structure.

To theoretically investigate the structural properties of P2-$K_{0.75}MNFO_2$, we performed first-principles calculations based on the structural information obtained by Rietveld refinement. For the calculation, we considered the P2-phase structure with an ABBA oxygen stacking sequence. Fig. 3a presents the formation energies of P2-K_xMNFO_2 as a function of the K content ($0 \le x \le 1$). The computational results indicate that P2-K_xMNFO_2 has sufficiently low formation energies to undergo a single P2-phase reaction during (de)potassiation. The detailed structural evolution of P2-K_xMNFO_2 was further investigated using *ex situ* and *in operando* XRD analysis, as discussed later in Fig. 4. On the basis of the formation energies, the approximate voltage profile of the P2-K_xMNFO_2 cathode was determined using the following equation:

$$V = -\frac{E[K_{x_2}MNFO_2] - E[K_{x_1}MNFO_2] - (x_2 - x_1)E[K]}{(x_2 - x_1)F} \quad (1)$$

where V is the average redox potential of the phase reaction between $K_{x_2}MNFO_2$ and $K_{x_1}MNFO_2$, and $E[K_xMNFO_2]$ is the formation energy of the most stable configuration of K_xMNFO_2. The predicted average redox potential of K_xMNFO_2 ($0 \le x \le 1$) was determined to be ~2.47 V (*vs.* K/K^+). As shown in Fig. 3b, we illustrated the predicted theoretical redox potential of P2-K_x-$MNFO_2$ ($0 \le x \le 1$) with the experimentally measured galvanostatic intermittent titration technique (GITT) profile in the voltage range of 1.5–3.9 V (*vs.* K/K^+). The result shows that the calculated voltage profile is in good agreement with the

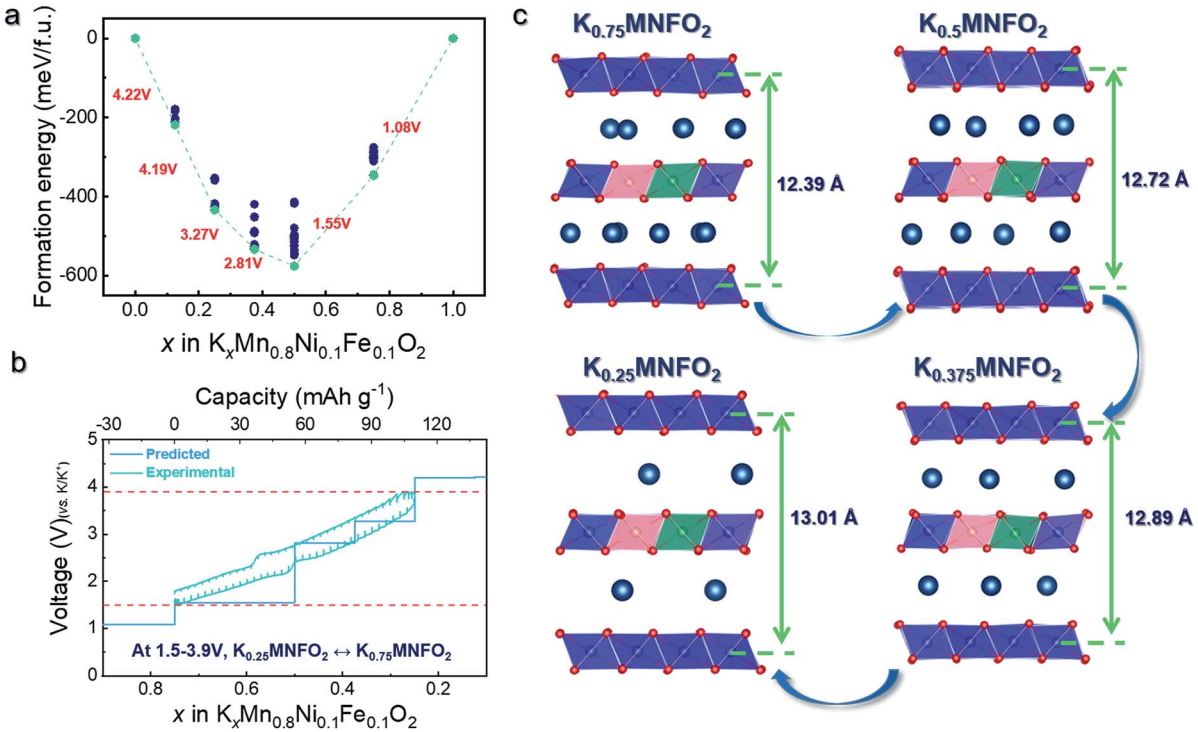

Fig. 3 (a) Formation energy of P2-K_xMNFO_2 ($0 \le x \le 1$), (b) GITT profile of P2-$K_{0.75}MNFO_2$ with its predicted redox potential, and (c) predicted structural change of P2-K_xMNFO_2 as a function of x content ($0.25 \le x \le 0.75$).

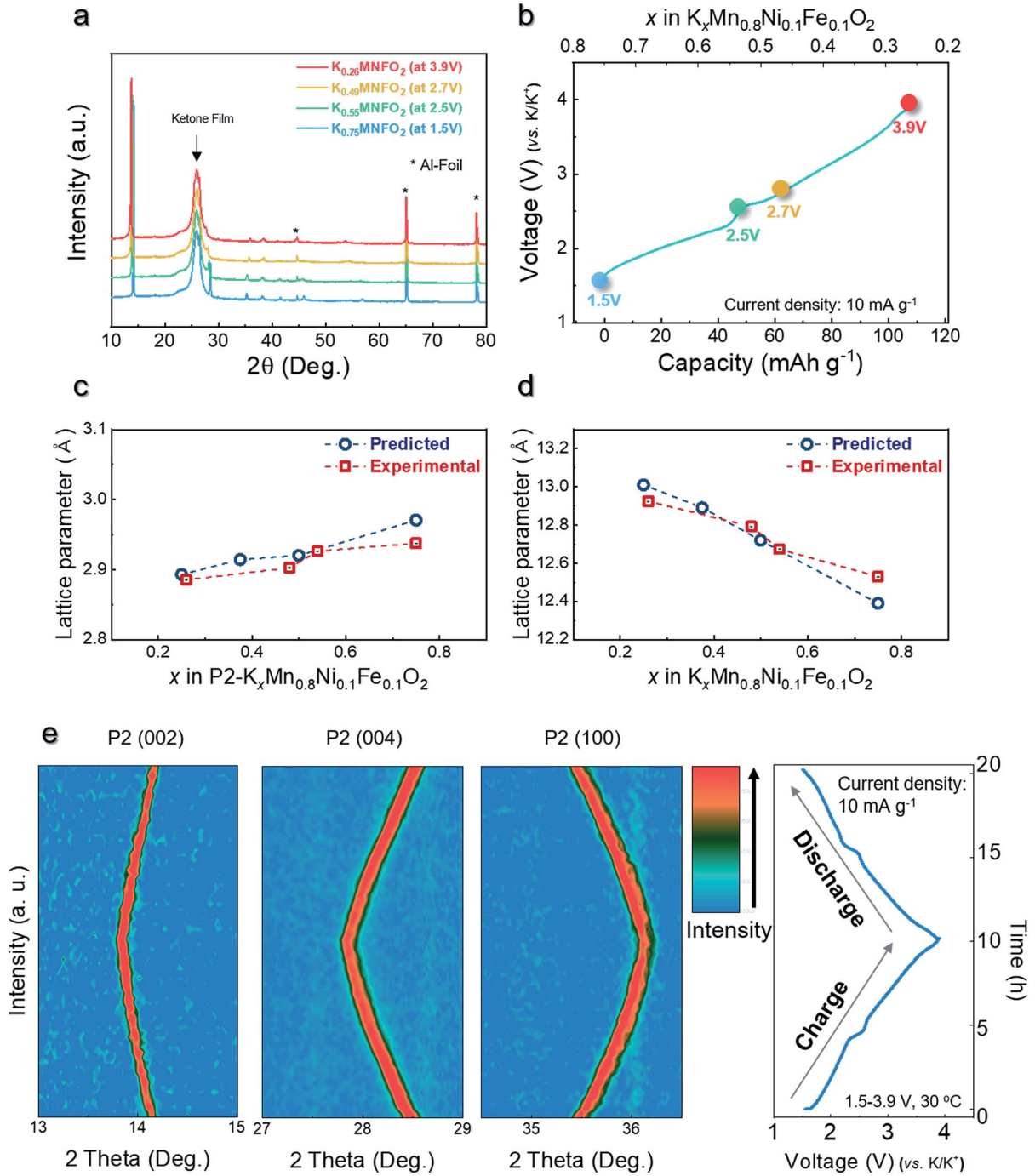

Fig. 4 (a) *Ex situ* XRD patterns of P2-K_xMNFO_2 ($0 \leq x \leq 1$) with (b) the associated charge curve. Lattice parameters (c) *a* and (d) *c* from experimentally calculated data and data predicted by first-principles calculations. (e) Contour maps in selected 2θ ranges obtained from *In operando* XRD patterns of P2-$K_{0.75}MNFO_2$ during the charge–discharge process in the voltage range of 1.5–3.9 V (K/K^+).

experimental voltage profiles. In addition, it was verified that ~0.5 mol of K^+ ions could be reversibly (de)intercalated into the P2-K_xMNFO_2 structure in the voltage range of 1.5–3.9 V (*vs.* K/K^+), which corresponds to a capacity of ~110 mA h g^{-1}. Structural stability is a key requirement for obtaining reversible behaviour, long cycle life, and power capability in intercalation electrode materials for KIBs. Thus, the crystal structure changes of P2-K_xMNFO_2 as a function of K^+ content ($x = 0.25$, 0.375, 0.5, and 0.75) were further investigated using the theoretical and experimental studies (Fig. 3c).

When K ions were extracted from P2-$K_{0.75}MNFO_2$ to P2-$K_{0.25}MNFO_2$, the *c* lattice parameter increased monotonously from ~12.39 to ~13.01 Å, respectively, because the *c* axis expanded and the *ab* plane contracted, owing to increased electrostatic repulsion between adjacent oxygen layers (O^{2-}–O^{2-}).[32] Even though a large amount of K^+ ions (~0.5 mol) are

deintercalated from the crystal structure during charging, P2-$K_{0.75}MNFO_2$ experienced small *c* lattice parameter changes of ~4.76%, indicating excellent structural stability. In order to confirm the computational data, the structural changes of P2-$K_{0.75}MNFO_2$ were examined using *ex situ* XRD measurement in different states of charge (Fig. 4a and b). The lattice parameter changes of P2-$K_{0.75}MNFO_2$ were calculated from the XRD data, and the results are overlaid on the computational data in Fig. 4c and d, indicating that the computed *a* and *c* lattice parameters agree well with the experimentally measured results. To gain more insight into the K storage behavior and changes in the crystal structure of P2-$K_{0.75}MNFO_2$ during the initial charge–discharge process, the structural evolution was further investigated by *in operando* XRD analysis. Contour maps in selected 2θ ranges are shown in Fig. 4e. In the initial state of charge, all the reflections of K_xMNFO_2 could be assigned to a pure P2-type layered phase.[31] Upon charging, the $(002)_{hex}$ and $(004)_{hex}$ diffraction lines shifted toward lower angles, whereas the $(100)_{hex}$ and $(103)_{hex}$ diffraction lines shifted gradually toward higher angles. The movement of all the diffraction peaks was reversible upon discharge. Note that no additional diffraction peaks beyond the P2-type structure were observed during the charge–discharge process in the voltage range of 1.5–3.9 V (*vs.* K/K^+); namely, unlike the K-based P2-type layered oxides reported to date,[19,31,33] P2-$K_{0.75}MNFO_2$ undergoes a single phase reaction in which ~0.5 mol of K^+ is extracted and inserted. Such reversible structural evolution demonstrated the sustainable and highly stable framework of P2-$K_{0.75}MNFO_2$. This observation using *in operand* XRD analysis was in good agreement with the reversible K extraction–insertion behaviour in the *ex situ* XRD patterns during the charge–discharge process for K_x-$MNFO_2$ in which *x* was varied between 0.25 and 0.75.

Cyclic voltammetry (CV) measurements of the P2-$K_{0.75}MNFO_2$ cathode were initially performed to obtain the general electrochemical response within the voltage range of 1.5–3.9 V (*vs.* K/K^+) at a scan rate of 0.1 mV s^{-1}. The CV plots in Fig. S5† revealed a series of peaks associated with the electrochemical processes involved in the redox couples and phase transformations during the entire charge–discharge process. The overlapping of the CV curves during cycling demonstrates good reversibility of K^+ insertion/extraction. Upon cycling, Fe^{3+}/Fe^{4+} redox reaction peaks are also observed at approximately 2.7/2.4 V in the CV curves. The reversible anodic/cathodic peaks at 3.85/3.7 V are attributable to the redox reaction of Ni^{2+}/Ni^{3+}. The pair of peaks at low voltage ~2.27 V (anodic scan)/1.6 and 2.05 V (cathodic scan) *vs.* K/K^+ are related to the redox reactions of Mn^{3+}/Mn^{4+}.[19,34–37] The charge compensation of P2-$K_{0.75}MNFO_2$ during charge–discharge was also investigated using *ex situ* X-ray absorption near edge structure (XANES) and X-ray photoelectron spectroscopy (XPS) measurements. For the present $K_{0.75}MNFO_2$ material, the resulting binding energies from the XANES spectra (Fig. S6†) were close to those of divalent Ni and trivalent Fe, while the binding energy of Mn was an intermediate value between those of trivalent (3+) and tetravalent (4+) Mn. The average oxidation state of transition metal elements such as Mn, Ni and Fe varies as the depotassiation proceeds with $Mn^{3+/4+}$ converting to Mn^{4+} and Ni^{2+} to Ni^{3+} and Fe^{3+} to Fe^{4+} at the end of charge.[38] As observed from *in operando*

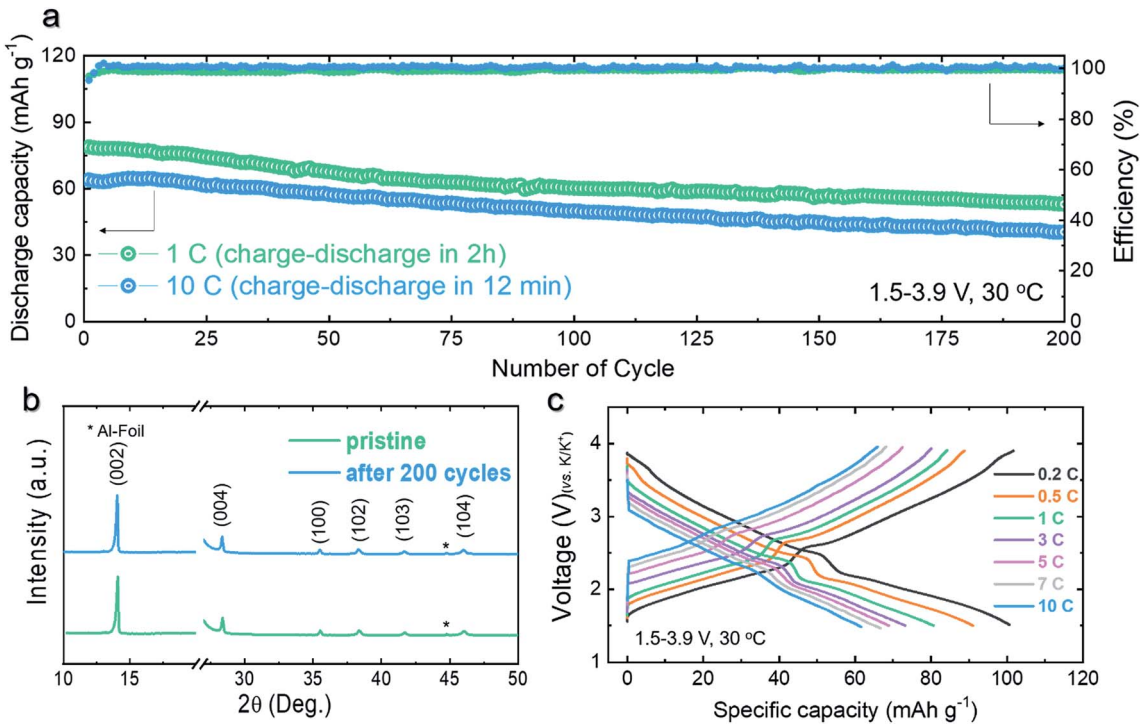

Fig. 5 (a) Cycle life test of the $K_{0.75}MNFO_2$ cathode in a half-cell at rates of 1C and 10C. (b) *Ex situ* XRD patterns of the pristine $K_{0.75}MNFO_2$ electrode and the electrode after 200 cycles at 10C. (c) Power capability of the $K_{0.75}MNFO_2$ cathode at various current rates from 0.2C to 10C.

XRD results, the original P2-type layer structure was recovered at the end of discharge and thus the average oxidation states of the transition metals are recovered to their original values in the XANES spectra. The binding energy changes in the XPS spectra (Fig. S7†) adequately confirm that ~0.5 mol of K^+ ions were intercalated into/deintercalated from the P2-$K_{0.75}MNFO_2$ cathode through the $Mn^{(3+/4+)}/Mn^{4+}$, Ni^{2+}/Ni^{3+} and Fe^{3+}/Fe^{4+} redox reactions.[39–45]

On the other hand, looking back to Mn-rich cathode materials, the removal and restoration of the Jahn–Teller distortions of Mn^{3+} during the charge–discharge process usually cause large stresses on the structure,[38] which are attributed mainly to the preferred elongation of the Mn–O distance in one direction in the octahedral environment in a highly occupied state with alkali ions. On the basis of previous reports, we speculated that dilution of the Mn^{3+} species in K_xMnO_2 compounds by partial substitution of Fe and Ni at Mn sites could effectively eliminate the cooperative effect of the Jahn–Teller ions.[46,47] To compare the effect of Jahn–Teller distortion resulting from Mn^{3+} ions, the Mn–O bond lengths of P2-K_xMNFO_2 and P2-K_xMnO_2 were investigated by first-principles calculations. As shown in Fig. S8,† the Mn′1–O′1 and Mn′1–O′6 bonds in P2-$K_{0.75}MnO_2$ are notably longer than the other bonds, whereas all the Mn–O bonds in P2-$K_{0.75}MNFO_2$ have similar lengths. This result implies that P2-$K_{0.75}MNFO_2$ may experience less irreversible structural distortion than P2-$Na_{0.75}MnO_2$, which ultimately leads to outstanding structural stability of P2-$K_{0.75}MNFO_2$ during repeated cycling. In the previous literature, it was reported that the Jahn–Teller distortion of Mn could affect the structural stability and cause a particular type of Na/vacancy ordering depending on the Na content of the Na_xMnO_2 structure, resulting in various steps in the voltage profile of Na_x-MnO_2.[48] Thus, we believed that the smooth voltage profile of P2-$K_{0.75}MNFO_2$ could be affected to a weakening of Jahn–Teller distortion of Mn by partial substitution of Fe and Ni.

As observed in the GITT curves in Fig. 3b, P2-$K_{0.75}MNFO_2$ delivered a high reversible capacity of 110 mA h g^{-1} at 0.1C (10 mA g^{-1}) in the voltage range of 1.5–3.9 V. Further, P2-$K_{0.75}MNFO_2$ exhibited a smooth voltage profile without the extent of multiple voltage steps in good agreement with the predicted data by first-principles calculation. Moreover, its sloping charge–discharge curve could be attributed to reversible structural evolution with a single-phase reaction during K^+ (de) intercalation. As verified by the highly stable K storage behaviour and changes in the crystal structure during the charge–discharge process, P2-$K_{0.75}MNFO_2$ demonstrated an outstanding cycle retention of ~70% over 200 cycles at 1C (Fig. 5a). Furthermore, to verify the power capability, we performed charge–discharge tests of the P2-$K_{0.75}MNFO_2$ cathode at various rates from 0.1C (10 mA g^{-1}) to 10C (1000 mA g^{-1}) in the voltage range of 1.5–3.9 V (Fig. 5c). The P2-$K_{0.75}MNFO_2$ cathode delivered a high reversible capacity of 62 mA h g^{-1} even at a rate of 10C (full charge–discharge in 12 min). Moreover, the P2-$K_{0.75}MNFO_2$ cathode delivered excellent cycling stability over

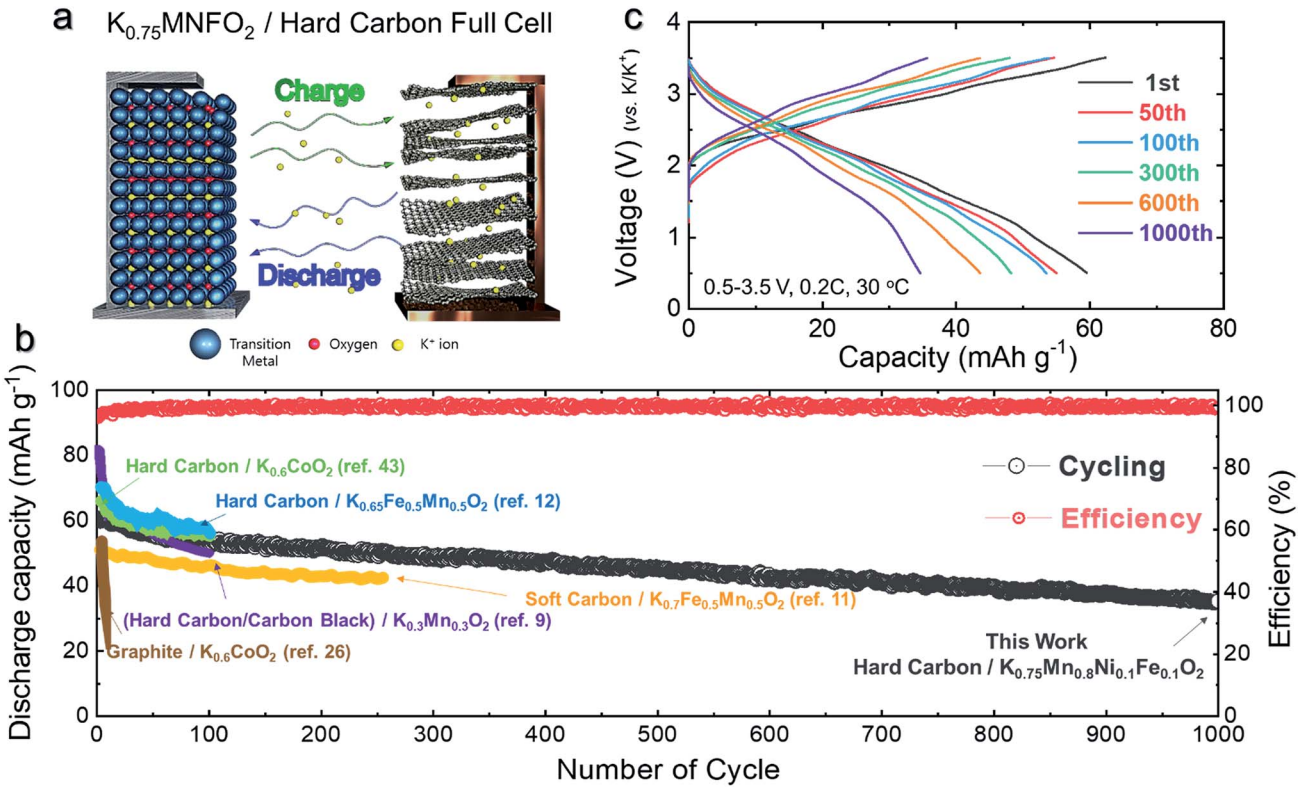

Fig. 6 (a) Schematic illustration of the $K_{0.75}MNFO_2$/hard carbon full cell. (b) Long-term cycling stability test of the hard carbon/$K_{0.75}MNFO_2$ full cell at 0.2C (20 mA g^{-1}) in the voltage range of 0.5–3.5 V and comparison of specific capacity *vs.* cycle umber for the reported full cells using layered oxide cathodes and carbon anodes. (c) Charge–discharge voltage profiles of the hard carbon/$K_{0.75}MNFO_2$ full cell.

200 cycles at 10C (Fig. 5a) and retained its original crystal structure well after cycling (Fig. 5b); these data further strengthen our conclusion that the electrochemical response of the P2-$K_{0.75}MNFO_2$ cathode reflects well the intrinsic structural stability of its active mass.

Because K metal is much more reactive than Li and Na metals, dendritic growth of K metal during repeated charge–discharge processes may cause serious safety issues.[49] Namely, the practical applicability of cells that use K metal directly in batteries cannot be guaranteed and thus development of K-ion full cells using a K-metal free anode was imperative for practical use in battery applications. Therefore, the K-ion full cell system using hard carbon as an anode is a suitable choice for practical use in battery applications because hard carbon can take up/release the K^+-ions during repeated cycling (Fig. S9†). Before the full cell assembly, the hard carbon anode was pre-cycled between 0.01 and 2.0 V (*vs.* K/K^+) to remove the irreversible capacity in the first cycle (Fig. S10†). Fig. 6a schematically illustrates the P2-$K_{0.75}MNFO_2$/hard carbon full cell. Fig. 6b shows the results of a long-term cycling test at a current rate of 0.2C (20 mA g^{-1}) in the voltage range of 0.5–3.5 V and comparison of specific capacity *vs.* cycle number for the reported full cells using layered oxide cathodes and carbon anodes.[9,11,12,26,43] The corresponding charge–discharge voltage profiles for the long-term cycling of the P2-$K_{0.75}MNFO_2$/hard carbon full cell are shown in Fig. 6c. The full cell delivered a high initial discharge capacity of 60 mA h g^{-1} and extremely stable long-term cycling, with ~60% capacity retention over 1000 cycles at 0.2C; to the best of our knowledge, the proposed full cell integrates state-of-the-art developments in KIB technology for use in a battery delivering a longer cycling performance than any yet reported. Finally, to better understand the excellent power capability of the P2-$K_{0.75}MNFO_2$ cathode observed in Fig. 5c, the diffusion pathways of K^+ ions and the activation barrier energy for K^+ ion diffusion between K sites in the *ab* plane were calculated using the nudged elastic band method.[29] As shown in Fig. 7a, $K_{0.75}MNFO_2$ has large two-dimensional K^+ ion diffusion pathways, which are highly advantageous for transport of the large K^+ ion during (de) potassiation. The predicted activation barrier for K^+ ion diffusion in the P2-$K_{0.75}MNFO_2$ structure is only ~580 meV (Fig. 7b). The value is sufficiently low for facile K^+ ion migration along the two-dimensional *ab* plane; thus, it supports well our experimental observation of the excellent power capability of P2-$K_{0.75}MNFO_2$.

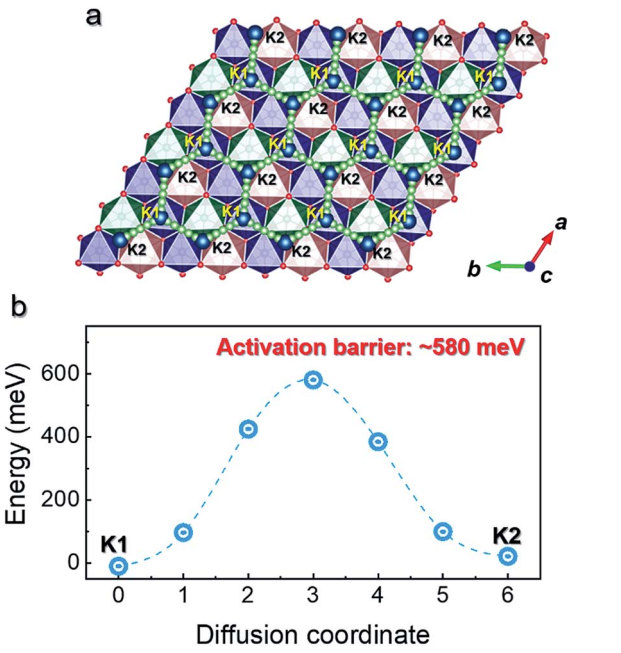

Fig. 7 (a) Schematic of predicted K^+ ion diffusion along the *ab* plane in P2-$K_{0.75}MNFO_2$ and (b) predicted activation barrier for K^+ ion diffusion into the P2-$K_{0.75}MNFO_2$ structure.

Conclusions

In summary, we synthesized P2-$K_{0.75}MNFO_2$ *via* an electrochemical ion-exchange route as a novel and low-cost Mn-based layered oxide cathode material for advanced KIBs. The electrochemical ion-exchange method provides two striking advantages for synthesizing K-based layered oxide cathode materials compared to the typical synthesis method. (1) We can use Li- or Na-based layered oxide compounds with relatively low sensitivity to air, resulting in less structural deterioration during the synthesis process. (2) It is also possible to use well-developed numerous layered oxide compounds; hence, we can explore and develop a variety of K-based layered oxide cathode materials. The overall electrochemical K storage mechanism of P2-$K_{0.75}MNFO_2$ was investigated using first-principles calculations and various experiments. Owing to its highly stable layered oxide framework, the P2-$K_{0.75}MNFO_2$ cathode experienced little structural change and no extent of multiple phase transitions during K^+ ion (de)intercalation in the voltage range of 1.5–3.9 V (*vs.* K/K^+), resulting in outstanding electrochemical performance. Specifically, the P2-$K_{0.75}MNFO_2$ cathode delivered a high reversible capacity of 110 mA h g^{-1} at 0.1C and exhibited an outstanding cycle retention of 70% over 200 cycles at both 1C and 10C. In addition, $K_{0.75}MNFO_2$ has large two-dimensional K^+ ion diffusion pathways with a low activation barrier for K^+ ion diffusion (~580 meV) so it exhibited excellent power capability up to 10C. A hard carbon/P2-$K_{0.75}MNFO_2$ full cell further demonstrated impressive electrochemical performance, with long-term cycling stability over 1000 cycles. Compared with previously reported layered oxide cathode materials for KIBs (Tables S4 and S5†), the presented potassium ion storage abilities of the P2-$KMNFO_2$ cathode showed a great competitiveness in terms of cyclability and power capability. We believe that our findings offer new guidelines for developing promising cathode materials that are inexpensive to produce and provide excellent performance in KIBs.

Conflicts of interest

There are no conflicts to declare.

Acknowledgements

This work was supported by a grant from the Human Resources Development program (No. 20184010201720) of the Korea Institute of Energy Technology Evaluation and Planning (KETEP), funded by the Ministry of Trade, Industry and Energy of the Korean government, and by the Global Frontier R&D Program (2013M3A6B1078875) at the Center for Hybrid Interface Materials (HIM), Ministry of Science, ICT & Future Planning.

Notes and references

1 International Energy Agency, *Global EV Outlook 2018: Towards cross-modal electrification*, *2018*, https://webstore.iea.org/global-ev-outlook-2018/, accessed: February 2019.
2 B. Scrosati, J. Hassoun and Y.-K. Sun, *Energy Environ. Sci.*, 2011, **4**, 3287.
3 K. Turcheniuk, D. Bondarev, V. Singhal and G. Yushin, *Nature*, 2018, **559**, 467.
4 P. G. Bruce, S. A. Freunberger, L. J. Hardwick and J.-M. Tarascon, *Nat. Mater.*, 2012, **11**, 19.
5 J.-Y. Hwang, S.-T. Myung and Y.-K. Sun, *Chem. Soc. Rev.*, 2017, **46**, 3529.
6 J. C. Pramudita, D. Sehrawat, D. Goonetilleke and N. Sharma, *Adv. Energy Mater.*, 2017, **7**, 1602911.
7 J.-Y. Hwang, S.-T. Myung and Y.-K. Sun, *Adv. Funct. Mater.*, 2018, **2**, 182938.
8 Z. Jian, W. Luo and X. Ji, *J. Am. Chem. Soc.*, 2015, **137**, 11566.
9 C. Vaalma, G. A. Giffin, D. Buchholz and S. Passerini, *J. Electrochem. Soc.*, 2016, **163**, A1295.
10 H. Kim, D.-H. Seo, J. C. Kim, S.-H. Bo, L. Liu, T. Shi and G. Ceder, *Adv. Mater.*, 2017, **29**, 1702480.
11 T. Sun, Z.-J. Li, H.-G. Wang, D. Bao, F.-I. Meng and X.-B. Zhang, *Angew. Chem., Int. Ed.*, 2016, **128**, 10820.
12 X.-L. Huang, R.-Z. Wang, D. Xu, Z.-L. Wang, H.-G. Wnag, J.-J. Xu, Z. Wu, Q.-C. Liu, Y. Zhang and X.-B. Zhang, *Adv. Funct. Mater.*, 2013, **23**, 4274.
13 H. Wnag, D. Ma, X. Huang, Y. Huang and X. Zhang, *Sci. Rep.*, 2012, **2**, 701.
14 Y.-H. Zhu, Q. Zhang, X. Yang, E.-Y. Zhao, T. Sun, X.-B. Zhang, S. Wang, X.-Q. Yu, J.-M. Yan and Q. Jiang, *Chem*, 2019, **5**, 168.
15 Y.-H. Zhu, X. Yang, T. Sun, S. Wang, Y.-L. Zhao, J.-M. Yan and X.-B. Zhang, *Electrochemical Energy Reviews*, 2018, **1**, 548.
16 Y.-H. Zhu, X. Yang, D. Bao, X.-F. Bie, T. Sun, S. Wang, Y.-S. Jinag, X.-B. Zhang, J.-M. Yan and Q. Jiang, *Joule*, 2018, **2**, 736.
17 Y.-H. Zhu, Y.-B. Yin, X. Yang, T. Sun, S. Wang, Y.-S. Jiang, J.-M. Yan and X.-B. Zhang, *Angew. Chem., Int. Ed.*, 2017, **56**, 7881.
18 T. Deng, X. Fan, J. Chen, L. Chen, C. Luo, X. Zhou, J. Yang, S. Zheng and C. Wang, *Adv. Funct. Mater.*, 2018, **28**, 1800219.
19 N. Navven, W. B. Park, S. C. Han, S. P. Singh, Y. H. Jung, D. Ahn, K.-S. Shon and M. Pyo, *Chem. Mater.*, 2018, **30**, 2049.
20 J.-Y. Hwang, J. Kim, T.-Y. Yu and Y.-K. Sun, *Adv. Energy Mater.*, 2019, **9**, 1803346.
21 J.-Y. Hwang, J. Kim, T.-Y. Yu, S.-T. Myung and Y.-K. Sun, *Energy Environ. Sci.*, 2018, **11**, 2821.
22 G. Kresse and J. Furthmüller, *Comput. Mater. Sci.*, 1996, **6**, 15.
23 P. E. Blöchl, *Phys. Rev. B: Condens. Matter Mater. Phys.*, 1994, **50**, 17953.
24 J. P. Perdew, K. Burke and M. Ernzerhof, *Phys. Rev. Lett.*, 1996, **77**, 3865.
25 V. I. Anisimov, F. Aryasetiawan and A. I. Lichtenstein, *J. Phys.: Condens. Matter*, 1997, **9**, 767.
26 A. Jain, G. Hautier, S. P. Ong, C. J. Moore, C. C. Fischer, K. A. Persson and G. Ceder, *Phys. Rev. B: Condens. Matter Mater. Phys.*, 2011, **84**, 045115.
27 A. Van der Ven, J. C. Thomas, Q. Xu and J. Bhattacharya, *Math. Comput. Simulat.*, 2010, **80**, 1393.
28 G. Henkelman, *J. Chem. Phys.*, 2000, **113**, 9901.
29 C. Delmas, J.-J. Braconnier, C. Fouassier and P. Hagenmuller, *Solid State Ionics*, 1981, **3/4**, 165.
30 Y. Hironaka, K. Kubota and S. Komaba, *Chem. Commun.*, 2017, **53**, 3693.
31 P.-F. Wang, H.-R. Yao, X.-Y. Liu, Y.-X. Yin, J.-N. Zhang, Y. Wen, X. Yu, L. Gu and Y.-G. Guo, *Sci. Adv.*, 2018, **4**, 1.
32 H. Kim, J. C. Kim, S.-H. Bo, T. Shi, D.-W. Kown and G. Ceder, *Adv. Energy Mater.*, 2017, **7**, 1700098.
33 N. Yabuuchi, M. Kajiyama, J. Iwatate, H. Nishikawa, S. Hitomi, R. Okuyama, R. Usui, Y. Yamada and S. Komaba, *Nat. Mater.*, 2012, **11**, 512.
34 J. Xu, S.-L. Chou, J.-L. Wang, H.-K. Liu and S.-X. Dou, *ChemElectroChem*, 2014, **1**, 371.
35 Y. Takeda, K. Nakahara, M. Nishijima, N. Imanishi, O. Yamamoto, M. Takano and R. Kanno, *Mater. Res. Bull.*, 1994, **29**, 659.
36 D. Yuan, X. Hu, J. Qian, F. Pei, F. Wu, R. Mao, X. Ai, H. Yang and Y. Cao, *Electrochim. Acta*, 2014, **116**, 300.
37 N. Yabuuchi, M. Yano, H. Yoshida, S. Kuze and S. Komaba, *J. Electrochem. Soc.*, 2013, **160**, A3131.
38 A. Davidson, J. F. Tempere and M. Che, *J. Phys. Chem.*, 1996, **100**, 4919.
39 F. Wu, J. Tian, Y. Su, J. Wang, C. Zhang, L. Bao, T. He, J. Li and S. Chen, *ACS Appl. Mater. Interfaces*, 2015, **7**, 7702.
40 J. Guo, X. Zhang, X. Du and F. Zhang, *J. Mater. Chem. A*, 2017, **5**, 6447.
41 C. V. Ramana, M. Massot and C. M. Julien, *Surf. Interface Anal.*, 2005, **37**, 412.
42 T. Yamashita and P. Hayes, *Appl. Surf. Sci.*, 2008, **254**, 2441.
43 R. Rajagopalan, B. Chen, Z. Zhang, X.-L. Wu, Y. Du, Y. Huang, B. Li, Y. Zong, J. Wang, G.-H. Nam, M. Sindoro, S. X. Dou, H. K. Liu and H. Zhang, *Adv. Mater.*, 2017, **29**, 1605694.
44 B. Mortemard de Boisse, D. Carlier, M. Guignard, L. Bourgeois and C. Delmas, *Inorg. Chem.*, 2014, **53**, 11197.
45 J. M. Paulsen and J. R. Dahn, *Solid State Ionics*, 1999, **126**, 3.
46 R. J. Clément, P. G. Bruce and C. P. Grey, *J. Electrochem. Soc.*, 2015, **162**, A2589.
47 S. Kumakura, Y. Tahara, K. Kubota, K. Chihra and S. Komaba, *Angew. Chem., Int. Ed.*, 2016, **55**, 12760.
48 N. Xiao, G. Gourdin and Y. Wu, *Angew. Chem., Int. Ed.*, 2018, **57**, 10864.
49 T. Deng, X. Fan, C. Luo, J. Chen, L. Chen, S. Hou, N. Edison, X. Zhou and C. Wang, *Nano Lett.*, 2018, **18**, 1522.

